

Estimation of Backscatter Coefficients Using an *In Situ* Calibration Source

Trong N. Nguyen¹, Member, IEEE, Alex J. Tam, Minh N. Do², Fellow, IEEE, and Michael L. Oelze¹, Senior Member, IEEE

Abstract—The objective of this article is to demonstrate the feasibility of estimating the backscatter coefficient (BSC) using an *in situ* calibration source. Traditional methods of estimating the BSC *in vivo* using a reference phantom technique do not account for transmission losses due to intervening layers between the ultrasonic source and the tissue region to be interrogated, leading to increases in bias and variance of BSC-based estimates. To account for transmission losses, an *in situ* calibration approach is proposed. The *in situ* calibration technique employs a titanium sphere that is well-characterized ultrasonically, biocompatible, and embedded inside the sample. A set of experiments was conducted to evaluate the embedded titanium spheres as *in situ* calibration targets for BSC estimation. The first experiment quantified the backscattered signal strength from titanium spheres of three sizes: 0.5, 1, and 2 mm in diameter. The second set of experiments assessed the repeatability of BSC estimates from the titanium spheres and compared these BSCs to theory. The third set of experiments quantified the ability of the titanium bead to provide an *in situ* reference spectrum in the presence of a lossy layer on top of the sample. The final set of experiments quantified the ability of the bead to provide a calibration spectrum over multiple depths in the sample. All experiments were conducted using an L9-4/38 linear array connected to a SonixOne system. The strongest signal was observed from the 2-mm titanium bead with the signal-to-noise ratio (SNR) of 11.6 dB with respect to the background speckle. Using an analysis bandwidth of 2.5–5.5 MHz, the mean differences between the experimentally derived BSCs and BSCs derived from the Faran theory were 0.54 and 0.76 dB using the array and a single-element transducer, respectively. The BSCs estimated using the *in situ* calibration approach without the layer and with the layer and using the reference phantom approach without the layer present. The mean differences in BSCs were 0.15, 0.73, and –9.69 dB, respectively. The mean differences of the BSCs calculated from data blocks located at depths that were either 30 pulse lengths above or below the actual bead depth compared to the BSC calculated at bead depth were –1.55 and –1.48 dB, respectively. The results indicate that an *in situ* calibration target can account for overlaying tissue losses, thereby improving the robustness of BSC-based estimates.

Index Terms—Backscatter coefficient (BSC), *in situ* calibration, quantitative ultrasound (QUS).

Manuscript received June 28, 2019; accepted September 24, 2019. Date of publication September 27, 2019; date of current version January 24, 2020. This work was supported by the NIH under Grant R21 EB020766 and Grant R21 EB020759. (Corresponding author: Trong N. Nguyen.)

The authors are with the Department of Electrical and Computer Engineering, Beckman Institute for Advanced Science and Technology, University of Illinois at Urbana–Champaign, Urbana, IL 61820 USA (e-mail: tnnguyen2@illinois.edu; oelze@illinois.edu).

Digital Object Identifier 10.1109/TUFFC.2019.2944305

I. INTRODUCTION

QUANTITATIVE ultrasound (QUS) techniques have demonstrated the ability to characterize tissues, classify disease state, detect cancer, and identify the response of cancer to therapy [1]–[7]. Among these techniques, spectral-based QUS utilizing the backscatter coefficient (BSC) has demonstrated success and continues to garner interest. In spite of the success of QUS to date, there remains a fundamental challenge with acquiring consistent QUS estimates when imaging *in vivo*, especially using the BSC. The challenge with a spectral-based estimation of the BSC *in vivo* is the inability in most cases to account for intervening losses between the transducer and the region of tissue to be interrogated. These losses can occur through transmission losses between different tissue layers and from frequency-dependent attenuation in the tissues.

Currently, two methods have been adopted for estimating the BSC: the planar reference technique [8]–[11] and the reference phantom technique [12], [13]. In both cases, an averaged power spectrum is acquired from raw radio-frequency (RF) backscattered ultrasound located spatially from a data block within a sample of tissue. The backscattered signals in the data block consist of several scan lines gated with a windowing function. The signals in the data block are assumed to arise from a random spatial arrangement of scatterers with uniform scattering statistics. To calculate the BSC, the averaged power spectrum is divided by a reference spectrum that accounts for the diffraction and system-dependent effects. The bias and variance of the BSC estimates depend on several factors, including the size of the data block used, the analysis bandwidth, the windowing function, and accounting for system-dependent effects and losses incurred between the transducer and data block [14]–[17].

Conventional methods of calibration for QUS require collecting signals from a well-characterized reference phantom or from a planar reflector, which are external to the tissue being imaged. The long-recognized problem with this approach is that the transmission losses and attenuation through intervening layers between the transducer and the data block are unknown. Currently, there is no method available to account for both the transmission losses and frequency-dependent attenuation that occur as ultrasound propagates through tissues. Several methods have been proposed to estimate the total attenuation to a tissue region [18]–[22]. However, these techniques suffer from large variance of estimates and do not account for transmission losses. In one recent paper, the variance of attenuation estimation was greatly reduced

by incorporating prior information into a regularization scheme [20]. In an interlaboratory comparison of the BSC estimation approaches, to enable accurate BSC estimates, the transmission coefficient was provided to the participants to account for losses induced by layers on the phantom materials used in the study [23]. Therefore, the interlaboratory study demonstrates the importance of accounting for transmission losses to obtain accurate estimates of the BSC.

The inability to account for these losses results in a reduction in the diagnostic capabilities of spectral-based QUS techniques. When scanning different tissues from different patients or even the same patient over time, the intervening layers between the transducer and the region of interest may not be the same. This can result in an increase in the variance of QUS estimates from one scan to the next and between different patients despite methods in hand to partially correct for attenuation. In spectral-based QUS techniques for tissue classification, it is important to reduce the variance of estimates [24], which improves the ability to uniquely classify a tissue or tissue state.

In this article, we demonstrate that an *in situ* calibration approach can provide improved estimates of BSCs by accounting for ultrasonic transmission losses and attenuation encountered in a tissue. Specifically, the proposed *in situ* calibration approach employs a biocompatible sphere embedded in the vicinity of a tissue to be scanned. Because the sphere is in the tissues being scanned, the sphere will encounter similar losses and diffraction as the investigated tissue and can be used to generate a reference spectrum to provide a more precise estimation of the BSC. The *in situ* calibration approach offers several advantages over techniques, such as in [18]. First, the *in situ* calibration technique allows compensation of transmission losses due to reflection/transmission through several layers, whereas the attenuation estimation techniques do not provide the ability to compensate for transmission losses. Second, the *in situ* calibration technique does not require a specific model for both attenuation and the BSC. Third, the *in situ* calibration technique does not require a large amount of data to reduce estimation variance. Example applications may include embedding spheres within a breast tumor during a biopsy and before chemotherapy. The current standard of practice before neoadjuvant chemotherapy is to embed fiducial markers into the breast tumor and lymph nodes suspected to contain cancer for future imaging. In these applications, the sphere would be used to register the tumor location and provide a calibration target that takes into account the overlaying layers. QUS could then be used to monitor the tumor or provide a means of identifying response of the tumor to therapy over time [25].

The purpose of the current study is to evaluate the performance of an *in situ* calibration bead for providing a reference spectrum for BSC estimation. Note that the purpose of the study is not to estimate the transmission and attenuation losses to some sample region but to account for these losses through a calibration target embedded in the sample. In this article, three important features of the new calibration approach were assessed. First, the strength of the signal was tested for a variety of bead sizes relative to a wavelength. Second,

the accuracy and repeatability of the BSC estimates from the bead were evaluated using a single-element transducer and a linear array from a clinical ultrasound system and size of the bead relative to the transducer beamwidth. Third, the ability to replace the external reference phantom in the presence of unknown transmission losses was assessed. Finally, the accuracy of the calibration procedure was quantified for BSC estimation in the tissue at different depths compared to the depth of the calibration bead.

II. THEORY

The BSC is defined as the differential backscattered cross-section per unit volume [26]. The scattered intensity, as a function of frequency, is estimated from an averaged power spectrum of the RF signal corresponding to ultrasound backscatter from a data block. The power spectrum can be calculated from each windowed scan line of the data block through the magnitude squared of the Fourier transform of the RF signal. Assuming a single scattering approximation and that the data block is at least one aperture diameter away from the transducer surface, the power spectrum can be represented as [27]

$$W(f, \mathbf{x}) = T(f, \mathbf{x})A(f, \mathbf{x})D(f, \mathbf{x})H(f, \mathbf{x})S(f, \mathbf{x}) \quad (1)$$

where $T(f, \mathbf{x})$ incorporates the transmission losses between tissues, $A(f, \mathbf{x})$ is the frequency-dependent attenuation, $D(f, \mathbf{x})$ represents the diffraction effects of the transducer, $H(f, \mathbf{x})$ is the impulse response of the transducer system and incorporates effects of the windowing function, the electro-mechanical response, and the time gain compensation (TGC), and $S(f, \mathbf{x})$ is the scattering function describing the underlying tissue microstructure. Note that each of the terms is spatially dependent.

The parameter of interest is the scattering function because it can be used to describe and possibly identify the state of the tissue. Therefore, it is necessary to account for all of the loss terms and system-dependent effects in the power spectrum estimate. Two methods have been adopted to account for the system-dependent effects in the power spectrum: 1) the planar reflector technique [8]–[11] and 2) the reference phantom technique [12], [13]. For the planar reflector technique, a smooth plate of known reflectivity is placed at the focus of the transducer and the signal from the reflector is recorded. Using the planar reflector signal as a reference will only account for $D(f, \mathbf{x})$ and $H(f, \mathbf{x})$ near the focus of a weakly focused source.

Similarly, the reference phantom technique utilizes the power spectrum from a well-characterized tissue-mimicking phantom to account for the system-dependent effects. Like the planar reflector technique, the reference phantom technique accounts for $D(f, \mathbf{x})$ and $H(f, \mathbf{x})$ but does not implicitly account for attenuation or transmission losses because the attenuation and transmission losses are, in general, unknown for a tissue *in vivo*. The attenuation correction in the reference phantom method can be incorporated through the backscatter-based attenuation estimation methods described earlier or by using values of attenuation for overlying layers

extracted from the literature. However, utilizing literature values of attenuation for different tissue layers still provides uncertainty for the exact corrections. The reference phantom technique can calibrate for system effects outside of the focus and for more highly focused sources, including array transducers using delay and sum beamforming. Therefore, the reference phantom technique is more versatile in the ability to calibrate for different transducer configurations; however, ensemble averaging is required to reduce the variance of the BSC introduced by the reference spectrum.

For an *in situ* calibration approach using a single spherical bead, the following assumptions are made. First, it is assumed that the signal, i.e., scattered intensity, from the calibration bead is much larger than the signal from the surrounding soft tissues (in our case we selected a bead that would be 10 dB above the background). Second, transmission and attenuation losses to the bead location in the tissue are close to the transmission and attenuation losses encountered at a similar depth in the tissue not containing the bead. This is valid when the tissue layers above the bead and above a data block to be analyzed are similar in thickness, number, and attenuation properties. The more this varies, the larger the error will be in the BSC estimate from the data block. Fig. 1 illustrates how the *in situ* calibration bead works in practice. The power spectrum from the bead is first acquired and then a power spectrum from a data block near the same depth as the bead in the sample is acquired. Under the two assumptions stated earlier, the power spectrum from the bead is given by

$$W_{\text{bead}}(f, \mathbf{x}) \approx T(f, \mathbf{x})A(f, \mathbf{x})D(f, \mathbf{x})H(f)S_{\text{bead}}(f, \mathbf{x}) \quad (2)$$

where $S_{\text{bead}}(f, \mathbf{x})$ is the scattering function from the calibration bead. Therefore, the BSC can be estimated by dividing the power spectrum of the sample by the power spectrum from the bead and multiplying by the BSC of the bead

$$\sigma_{\text{bsc}}(f, \mathbf{x}) = \frac{W(f, \mathbf{x})}{W_{\text{bead}}(f, \mathbf{x})} \sigma_{\text{bsc}}^{\text{bead}}(f, \mathbf{x}). \quad (3)$$

By estimating the power spectrum from the bead and utilizing the BSC from the bead, estimates of the BSC from a tissue can be acquired with the system-dependent terms, transmission losses, and frequency-dependent attenuation approximately taken into account. Once the BSC of a bead of known size and material is estimated, that BSC can be used in subsequent experiments without having to take additional BSC estimates each time that type of bead is used.

III. EXPERIMENTAL METHODS

In the first set of experiments, titanium spheres of sizes 0.5, 1, and 2 mm in diameter were purchased (BalTec, Los Angeles, CA, USA). These spheres are biocompatible and compatible with magnetic resonance imaging (MRI), making them desirable for clinical applications. The spheres were embedded in the middle of the tissue-mimicking phantoms. A phantom was made of 200 mL of degassed water and 5 g of noble agar powder. The signal intensity from the titanium bead was calculated and compared to the background speckle.

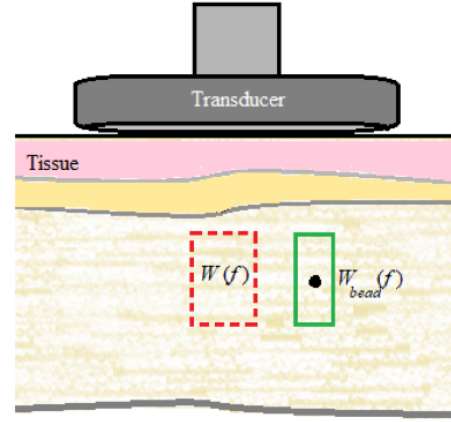


Fig. 1. Illustration of the *in situ* calibration technique. A transducer captures signal from a data block inside a tissue and the power spectrum is calculated from the backscattered ultrasound signal, $W(f)$. Signals are also captured from the *in situ* calibration bead located at a similar depth as the data block of tissue signal.

Specifically, we calculated the SNR as

$$\text{SNR} = 10 \log \left(\frac{\sigma_{\text{bead}}^2}{\sigma_{\text{speckle}}^2} \right) \quad (4)$$

where σ_{bead}^2 and $\sigma_{\text{speckle}}^2$ are the variances of the envelope signal at the bead location and of the speckle background, respectively. To calculate the SNR, the variance was calculated from the envelope data from a block surrounding the bead and surrounding a bead-free region at the same depth. The block size was 5 mm \times 5 mm. The smallest titanium bead that was 10 dB above the background tissue signal was chosen as the calibration bead for subsequent experimental evaluation. The 10 dB was chosen because it allowed us to utilize the analysis bandwidth of our transducer.

In the second set of experiments, BSCs were estimated from measurements from the titanium bead selected from the first set of experiments and compared to the Faran theory [28]. A single-element transducer and the first phantom were submerged in a water tank (see Fig. 2 for illustration). The phantom was scanned in order to isolate the scattering from the calibration bead alone to compare with theory, i.e., the Faran theory. The single-element transducer was an f/3 6-MHz focused transducer with a focal length of 2.25 in (or 57.15 mm). The beamwidth was estimated to be 0.771 mm. The bead was at a depth of 35 mm from the top surface of the phantom as confirmed by B-mode imaging of the phantom. The focused transducer was connected to a Panametrics 5800 pulse/receiver (Olympus NDT, Waltham, MA, USA) to excite the transducer and record the received data via a UF3 A/D card (Strategic Test, Boston, MA, USA) sampled at 250 MHz. After scanning the phantom, the transducer scanned a planar reflector (a piece of plexiglass) at the same depth as the calibration bead in the phantom to obtain a reference spectrum. The planar reference was used to remove the diffraction and system effects in order to compare the scattering from the titanium bead to the Faran theory for scattering from a sphere. The properties used for the Faran model and titanium were mass density (4.5 g/cc), Poisson's ratio (0.34), and sound speed

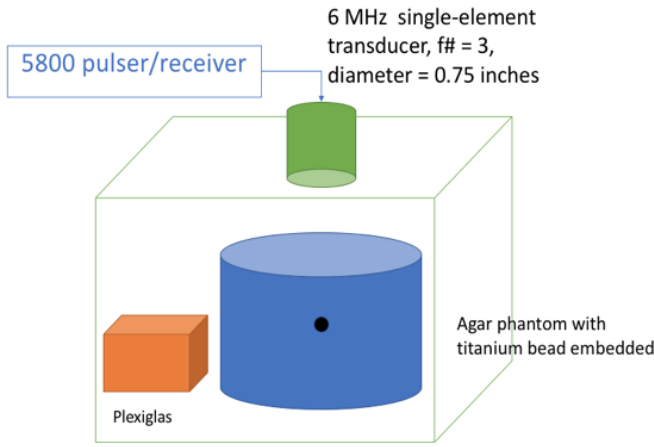


Fig. 2. Experimental testing configuration for estimating BSC from titanium bead.

(6100 m/s). A -10 -dB analysis bandwidth of 2.5 – 5.5 MHz was used. Next, the linear array was used to scan the same phantom to estimate the BSC of the bead, which subsequently was used as a calibration spectrum for later experiments. A reference phantom with known attenuation and BSC was scanned with the same system setup to remove the diffraction and system effects [29]. The array was touching the phantom surface. The experimental configuration was taken down and set up three separate times to test the repeatability of the BSC estimates from the bead.

In both experiments with the single-element and the linear array, the attenuation of the phantom was first estimated using the spectral difference method [30] to be $\alpha(f) = 0.2826f^{1.249}$ (dB/cm), which was then used to compensate for the losses in the phantom to the depth of the bead for the estimation of the BSCs. The differences between the BSCs estimated from the sphere using either the single element or the array compared to the Faran theory were calculated. Following [11], the fit between two BSCs was quantified using the first and second moments of the difference function:

$$D(\sigma_{\text{bsc1}}(f, x), \sigma_{\text{bsc2}}(f, x)) = 10 \log_{10} \frac{\sigma_{\text{bsc1}}(f, x)}{\sigma_{\text{bsc2}}(f, x)} \quad (5)$$

where $\sigma_{\text{bsc2}}(f, x)$ was taken to be the baseline. The functions D_σ and D_μ were defined as follows:

$$D_\mu(x) = \frac{1}{N} \sum_{i=1}^N D(\sigma_{\text{bsc1}}(f_i, x), \sigma_{\text{bsc2}}(f_i, x)) \quad (6)$$

$$D_\sigma(x) = \sqrt{\frac{1}{N} \sum_{i=1}^N [D(\sigma_{\text{bsc1}}(f_i, x), \sigma_{\text{bsc2}}(f_i, x)) - D_\mu(x)]^2} \quad (7)$$

where the averaging was over the analysis bandwidth. The quantities D_μ and D_σ are the measures of the amplitude- and frequency-dependence agreements between the two BSCs $\sigma_{\text{bsc1}}(f, x)$ and $\sigma_{\text{bsc2}}(f, x)$.

In the third set of experiments, the titanium bead selected from the first experiment was implanted in a homogenous tissue-mimicking phantom with glass beads or in a chicken breast phantom. The glass bead phantom was fabricated similar to the graphite phantoms from the first experiments except

that 2 g of glass beads (of size 50 – $90 \mu\text{m}$) were also added as a source of speckle to mimic *in vivo* conditions and have a ground truth for estimates of scatterer size. In the chicken breast phantom, the chicken breast was suspended in agar to provide extra depth from the phantom surface. The glass bead phantom and chicken breast phantom were scanned using the L9-4/38 array transducer connected to the SonixOne system with and without a layer of fatty pork placed between the transducer and the phantom. The chicken and pork samples were purchased from a local grocery store and kept in cold storage until preparation for scanning. The local attenuation of the phantom material was estimated using the spectral difference method [30] to be $\alpha(f) = 0.14184f^{1.7975}$ (dB/cm). Local attenuation estimation within the fatty layer could not be obtained using the method from [30] because we could not obtain sufficient-sized data blocks with uniform scattering within the fatty layers. BSCs from the samples were from data blocks at the same depth as the calibration bead in the sample. The BSCs were calculated from the data blocks of size nine beamwidths (10 mm) laterally by 30 pulse lengths axially (10 mm). BSCs were calculated with and without the layers on top and using the bead as a calibration target and the traditional reference phantom technique. The BSCs were compared between the different calibration approaches, and the differences of the BSCs were computed between the estimates with and without the layers present using (5). The baseline BSC was the BSC calculated without the layer and using the reference phantom. For the glass bead phantom, the effective scatterer diameter (ESD) of the glass beads was estimated using the Faran theory and the minimum average squared deviation approach [10].

In the final set of experiments, the same phantoms were used to quantify the error in the BSC estimate when the depth of the data block used for analysis was either at a greater depth or shallower depth than the titanium bead. The data block location was stepped from one full data block axial length above the bead to one full data block axial length below the bead depth (see Fig. 3). The upper data block was within the depth of field of the imaging array, and the lower data block was just outside of the depth of field. To account for the differences in the total attenuation of the data blocks at depths different from the bead depth, the total attenuation loss was assumed to be accounted for up to the bead depth and only the local attenuation corrections were needed to account for the offset of the data block from the bead depth. The local attenuation of the phantom was estimated using the spectral difference method [30]. Estimates of the BSC were acquired with and without the fatty layers on top and using the titanium bead as a reference and using the reference phantom technique. The mean differences between the BSCs estimated at the depth of the calibration bead and BSCs estimated at different depths were calculated using (5).

IV. RESULTS

Fig. 4 shows the B-mode images of the three different titanium beads (0.5-, 1-, and 2-mm diameter) embedded in graphite and agar phantom. The intensity of the signal scattered from each bead was calculated and compared to the

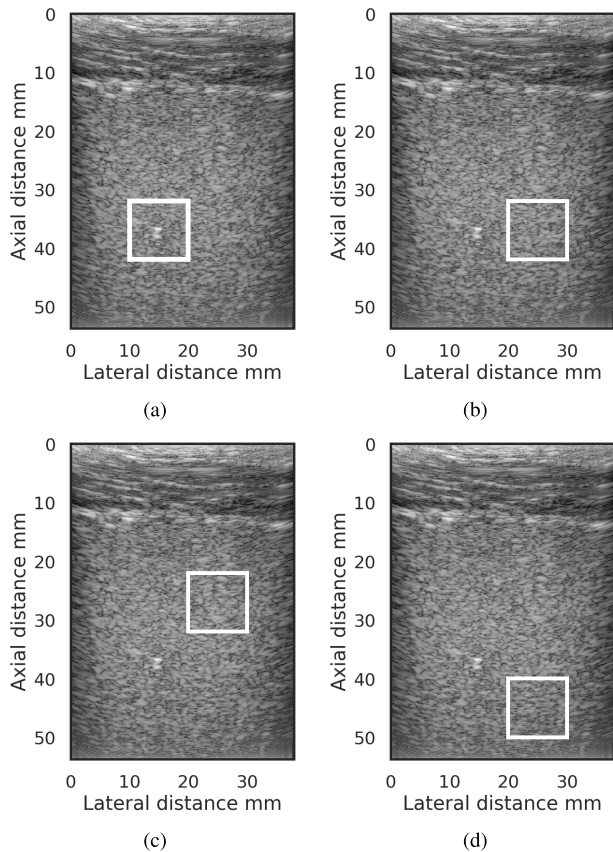


Fig. 3. (a) Data block around the bead to calculate the reference spectrum. (b) Data block to calculate the BSC at bead depth. (c) and (d) Data blocks above and below the bead to compare with BSC estimates from (b). The dynamic range of the images was 60 dB.

TABLE I
SNR VALUES FROM SIGNALS SCATTERED FROM THE TITANIUM
BEADS IN THE PHANTOMS FROM FIG. 5

Bead diameter	SNR
0.5 mm	2.65 dB
1 mm	5.69 dB
2 mm	11.61 dB

background speckle at the same depth. Table I lists the values of the SNR for each bead size in the phantom computed using (4). From the B-mode images shown in Fig. 4, the larger the bead size, the more visible the target. Based on the results from the SNR for each bead size examined, the 2-mm-diameter titanium bead with an SNR of 11.61 dB was chosen for subsequent experiments. In addition to the SNR values, when there are fatty pork layers on top of the phantoms or the bead is embedded inside the chicken breast, the 2-mm-diameter bead was also more visible and distinct compared to other small hyperechoic targets in the samples.

The BSCs for the 2-mm-diameter titanium bead acquired using the single-element transducer and the linear array are plotted in Fig. 5(a) along with a curve derived from the Faran theory. The BSC estimated using the single-element transducer was derived from power spectra averaged across a $2 \text{ mm} \times 2 \text{ mm}$ grid centered at the bead with the lateral step size of $100 \mu\text{m}$. The data block for BSC estimate using

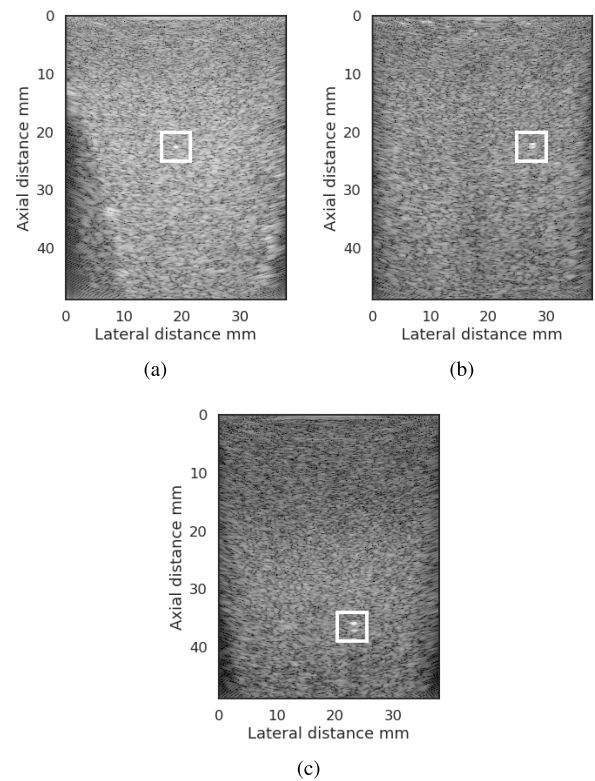


Fig. 4. B-mode images from phantoms embedded with (a) single 0.5-mm titanium bead, (b) 1-mm-diameter titanium bead, and (c) 2-mm-diameter titanium bead.

the array was $10 \text{ mm} \times 10 \text{ mm}$. Although the beamwidths of the single element and the linear array were estimated to be 0.771 and 1.11 mm, respectively, which are smaller than the bead size, the measured BSC captured most of the features of the curve predicted by the Faran theory. The mean differences of the BSCs between the Faran curve fit and the BSCs of the single-element transducer and the linear array were 0.76 and 0.54 dB, respectively. Fig. 5(b) shows the mean and standard deviation of the BSC of the titanium bead estimated using the linear array with the reference phantom technique where the experiment was repeated three times (over a period of two weeks).

Fig. 6 shows the B-mode images of the tissue-mimicking phantom containing the titanium bead with and without a fatty layer placed on top of the phantom. The layer acted to change the transmission and attenuation losses to the data block used for analysis. The attenuation of the fatty layer was estimated using a substitution method and found to be $1.04 \text{ dB} \cdot \text{MHz}^{-1} \cdot \text{cm}^{-1}$. The BSC was calculated for the phantom using the calibration bead and the reference phantom approach. The estimated ESD values are provided in Table II. The ESD was averaged from three data blocks centered at the same depth as the bead, and the standard deviation was calculated from the three ESD estimates. Using a Kruskal–Wallis test, no significant differences were observed between the ESDs estimated using the bead with a layer present and the ESDs estimated using the reference phantom with no layers present. In addition, mean differences for the BSCs between the different calibration approaches (compared

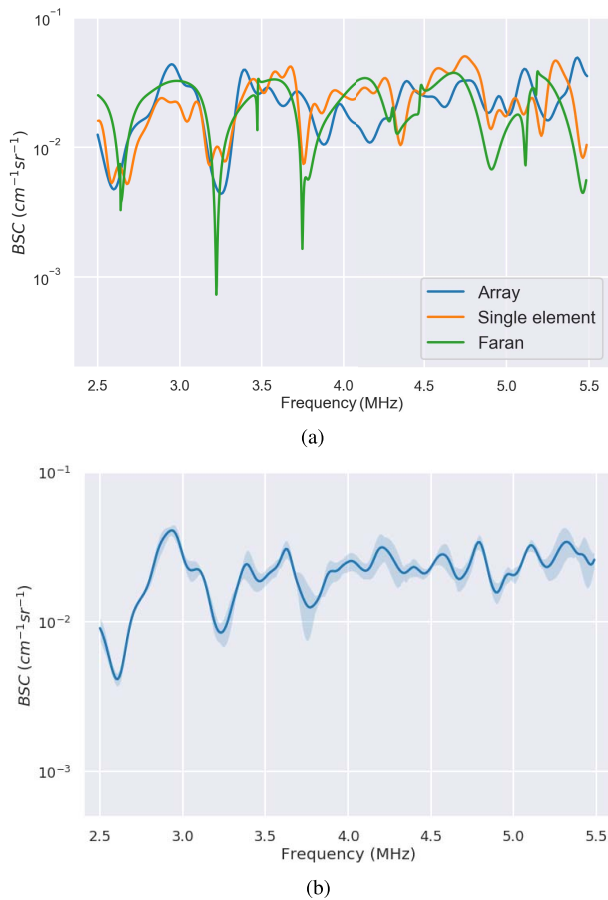


Fig. 5. (a) Comparison of the Faran theory of scattering from a 2-mm-diameter titanium sphere compared with the measurements from the sphere using a single-element transducer and from using the linear array L9-4/38. (b) Mean and standard deviation of the BSCs of the bead measured by the linear array over three different experimental time points.

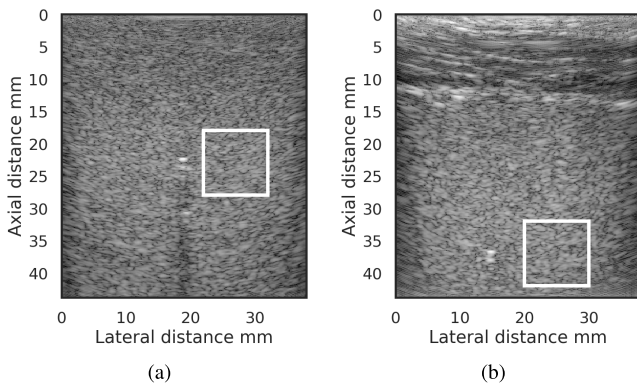


Fig. 6. B-mode images of phantoms (a) without and (b) with the layer on top.

to the baseline of the BSC calculated with no layers present and using the reference phantom) are also listed in Table II.

Plots of the BSCs versus the calibration approaches are provided in Fig. 7. Fig. 7 shows the BSCs estimated using the traditional reference phantom technique and the *in situ* calibration approach and with and without the layers present. The BSCs estimated using the *in situ* calibration approach

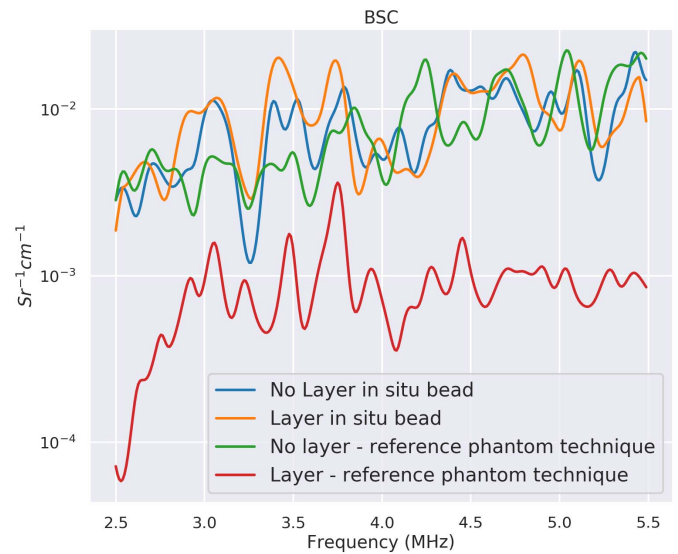


Fig. 7. BSCs from phantom using calibration bead and reference phantom technique.

with and without the layers present overlapped with the BSC estimated using the traditional reference phantom approach without the layer present. The BSC estimated using the traditional reference phantom approach with the layer present, without attempting to correct for attenuation and transmission losses through the layer, did not overlap with the other curves. The BSC using the traditional reference phantom technique (red curve), without layer attenuation correction, was underestimated when the fatty layer was placed on top. Use of attenuation and transmission correction, either through attenuation estimates from the backscatter or through the use of literature values of attenuation, would make the BSC curve closer to the BSC curves estimated without the lossy layer present. However, the BSC using the *in situ* calibration bead (orange curve) when the layer was on top was close to the BSC estimates without the fatty layer.

A B-mode image from a chicken breast having an embedded 2-mm-diameter titanium bead is shown in Fig. 8 with a fatty layer placed on top. BSC estimates from the chicken breast are provided in Fig. 9 using the reference phantom and calibration bead approaches with and without a fatty layer placed on top. The mean differences of the BSC estimates are provided in the last column of Table II. The SNR of the bead estimated from the chicken breast was 11.7 dB. Estimates of the BSC when varying the interrogation depth are provided in Fig. 10. The mean differences between BSCs calculated at the same depth of the calibration bead and at different depths are provided in Table III.

V. DISCUSSION

Currently, the reference phantom technique is the gold standard for the acquisition of a calibration spectrum for calculating the BSC when using a clinical system and an array probe. However, the reference phantom technique for estimating the spectral-based QUS parameters can result in high bias and high variance in QUS parameters due to the inability to account for the losses incurred from intervening layers.

TABLE II
ERROR ESTIMATES AND ESTIMATED GLASS BEAD CHARACTERISTICS USING THE DIFFERENT
REFERENCE TECHNIQUES WITH AND WITHOUT THE LAYERS PRESENT

	ESD (glass bead phantom)	D_μ (glass bead phantom)	D_σ (glass bead phantom)	D_μ (chicken phantom)	D_σ (chicken phantom)
No layer - reference phantom (baseline)	75.2 ± 1.7	0	0	0	0
No layer - <i>in situ</i> bead	71.2 ± 1.6	0.15	2.29	-3.71	2.32
Layer - <i>in situ</i> bead	76.5 ± 0.9	0.73	3.19	0.46	3.71
Layer - reference phantom	45.5 ± 4.0	-9.69	3.08	-10.19	4.71

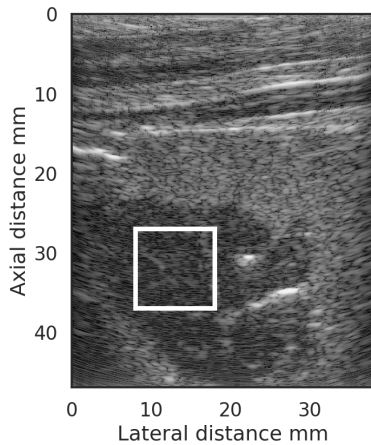


Fig. 8. B-mode of titanium bead in a chicken breast sample.

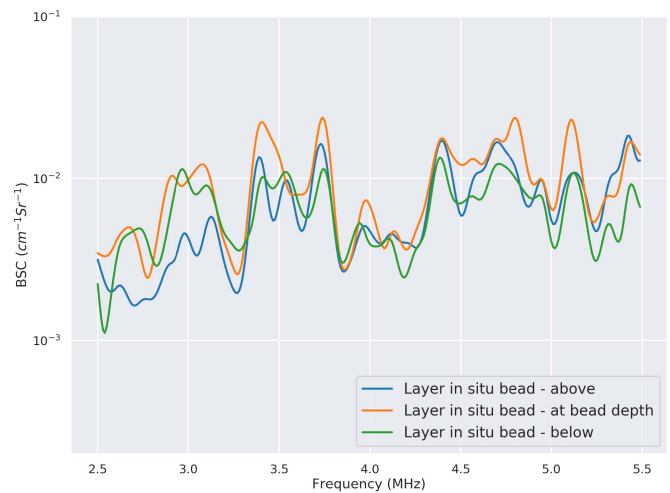


Fig. 10. BSCs from data blocks located at different depths relative to the bead depth.

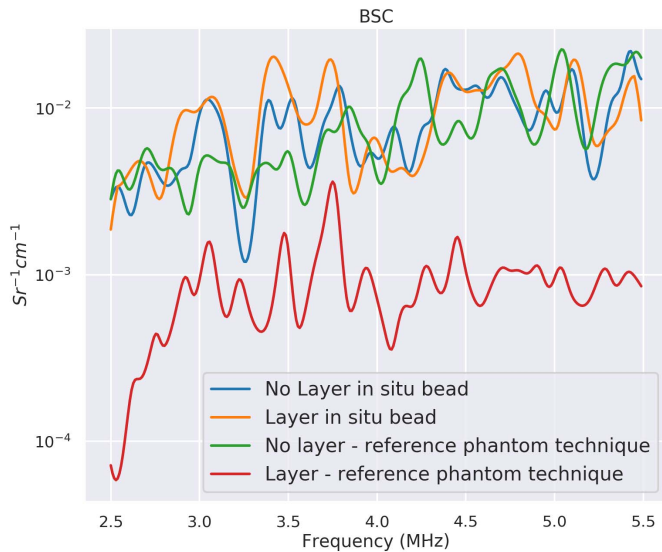


Fig. 9. BSCs from chicken breast using calibration bead and reference phantom technique.

The *in situ* calibration technique presented in this article removes the need to use a reference phantom in cases where an embedded bead could be used. The embedded bead can also be used to compensate for the attenuation and transmission losses at depth due to intervening layers. To evaluate the suitability of an *in situ* calibration target for spectral-based QUS analysis, we scanned titanium beads embedded in different samples with and without lossy layers placed on top of the samples.

In the first set of experiments, we assessed the importance of bead size on the ability to acquire sufficient SNR. The SNRs for the smaller beads, 0.5- and 1-mm diameter, were not sufficient to get good QUS estimates. These beads are also difficult to handle due to their size and not easily differentiated in the B-mode images from other impurities or structures giving rise to large specular signals. Therefore, our results suggest that a bead size of at least 2 mm be used. The SNR for the 2-mm titanium sphere was also confirmed in the chicken with a value of 11.7 dB, which suggests that smaller beads might not have been clearly visible in the chicken breast.

In the next set of experiments, the ability to accurately estimate a BSC from the embedded bead compared to theory was assessed. Overall, as Fig. 5(a) demonstrates, we were able to accurately estimate the BSC from the embedded 2-mm-diameter titanium bead. The BSC accuracy was observed even though the bead was larger than the beamwidth of the transducer (−6-dB pulse-echo beamwidths of the single element and linear array are estimated to be 770 μm and 1.1 mm, respectively). The 3-dB standard deviation of the error function was due to the sharp dips in the theoretical Farn curve, which were not as prominent in the measured BSCs of the bead, which makes it suitable to use as a reference spectrum. The BSC calculated from measurements from the bead in Fig. 5(a) contains noise and does not always match the theoretical BSC from the bead, especially near 5.5 MHz where the signal energy is closer to

TABLE III
ERROR ESTIMATES BETWEEN THE BSC AT BEAD DEPTH AND
BSCs ABOVE AND BELOW THE BEAD DEPTH

	D_{μ} (dB)	D_{σ} (dB)
BSC at bead depth (baseline)	0	0
BSC above the bead	-1.55	1.56
BSC below the bead	-1.48	1.42

the noise floor. For the reference phantom technique, noise in the reference spectrum can be reduced by averaging over many independent scan lines. This is not possible with the calibration bead. On the other hand, the noise present in the BSC of the bead can be characterized by high-frequency oscillations on top of a smoother BSC curve. Parameterization of the BSC for estimates, such as the ESD, typically involves fitting a slope to the BSC, which in effect low-pass filters the BSC curve. Therefore, the nature of the noise added from the bead spectrum has little effect on the accuracy of estimates of ESD, as shown in Table II.

Previous results from [31] demonstrated that accurate estimates of the BSC from large scatterers compared to a beamwidth could be acquired as long as the power spectrum was averaged from scan lines that traversed across the lateral length of the scatterer. Kemmerer *et al.* [31] demonstrated this effect with caviar eggs that are fluid spheres that supported little to no shear wave. The titanium bead did support a shear wave contribution to the scattering, as accounted for in the Faran theory. Therefore, the present results demonstrate that accurate BSCs can be estimated from high-contrast scatterers that are larger than a beamwidth and that support shear waves. These results suggest that the use of a large bead *in situ* for calibration is acceptable because it: 1) provides larger SNR than a smaller bead and 2) can provide accurate estimates of BSC at depth, assuming the beams traverse the width of the bead in the imaging field. The BSC measured from the bead using the linear array was also shown to be highly repeatable, i.e., the mean standard deviation of the BSCs across experiments was 1.32 dB.

In the third set of experiments, we assessed the performance of the *in situ* calibration approach compared to the traditional reference phantom approach when lossy layers were placed on top of samples. The experimental results for the phantoms indicated that the reference phantom technique, without attenuation correction, could not faithfully reproduce the BSC when a fatty layer was placed on top of the phantom samples. The presence of the layer caused the BSC from the reference phantom to both change its shape, i.e., slope, and overall magnitude, i.e., the magnitude of the BSC was lower. The mean differences of the BSCs, using the BSC from the reference phantom without a layer as baseline, were 0.15, 0.73, and -9.69 dB using the *in situ* calibration approach without the layer and with the layer and using the reference phantom approach with the layer, respectively. When using the *in situ* calibration bead, only small changes in the BSC were observed between the estimates of BSC with and without the layers present. Therefore, the use of the *in situ* calibration target

provided the ability to account for losses incurred from the lossy layer. Similar results were observed for BSC estimates from the chicken breast sample. In addition, the layer above the phantom was approximately 1 cm in thickness, whereas the fatty layer above the chicken was almost 1.5 cm and a small agar layer was also between the fatty layer and the chicken. This confirms that the *in situ* calibration approach can handle different layer thicknesses and multiple layers.

In the final set of experiments, we quantified the errors in the BSC that accumulate when the data blocks used for estimating the BSC occurred at different depths from the bead depth, i.e., the distance between the probe surface and the bead. The differences in the BSCs from the data blocks located at different depths were small compared to the data block centered at the bead depth (see Table III). These findings suggest that over a limited range, the *in situ* bead could properly account for losses, system effects, and diffraction effects in a homogeneous scattering region. The depth ranges over which the calibration from the bead is usable will depend on the specific scan configurations of the probe (e.g., focal properties). Because there can be a large number of possible focal and scan configurations with an array probe, we limited our analysis to simple linear sequential scanning with constant f-number focusing. These results demonstrate the versatility of the *in situ* calibration approach.

The limitation of the study lies in the assumption that the transmission and attenuation losses at the bead location are close to the transmission and attenuation losses of the data block in the sample under investigation. Ideally, the data blocks around the bead and for the interrogated sample are close axially and laterally. Axially, the transmission losses can be assumed to be constant, and only the local attenuation needs to be estimated. In Fig. 10, the local attenuation was compensated based on estimated local attenuation at the bead depth multiplied by the depth difference between the data blocks. The BSCs from the data block above and below the data block at the bead depth in Fig. 10 are similar, which shows that the local attenuation compensation is accurate. However, the local attenuation in the phantom is uniform and simpler to estimate compared to the attenuation changes in *in vivo* conditions, which might be difficult to estimate and could introduce error in the BSC estimation. Laterally, as the distance between the interrogated data block and the bead increases, the corrections for the transmission and attenuation losses may grow worse. The quality of the correction will depend on the shape of the overlying layers for the particular imaging task. For layers of constant thickness, the corrections from the bead would potentially be valid for greater distances laterally.

Finally, the *in situ* calibration approach in this article was not evaluated *in vivo*. The implantation of a bead *in vivo* can cause inflammation and fibrous growth around the marker location. If the bead size is on the order of the size of the lesion, scar tissue from the bead placement and inflammation may radically alter the tissue characteristics of the lesion being examined. Because the bead is made of metal and has a much higher impedance than the surrounding tissue, local changes in tissue microstructure due to the bead placement should not

greatly affect the ability to get signal from the bead. Future studies *in vivo* should include the analysis of the effects of the bead on local microstructure and how this could affect estimates of the BSC. However, currently biocompatible metal fiducial markers of similar size are already placed in tumors for image registration purposes without much concern for tissue effects [32], [33].

VI. CONCLUSION

In this article, we evaluated the performance of an *in situ* calibration bead for calculating the BSC. The important feature of the *in situ* calibration bead is the ability to account for transmission and attenuation losses due to intervening tissue layers between the region of interest and the transducer surface. Accounting for these losses will reduce variance in QUS estimates from one sample to the next. The performance of the bead approach was assessed versus bead size relative to a beamwidth and wavelength and the depth of the bead in the sample. The results indicate that the *in situ* calibration bead provides robust calibration spectra. The *in situ* calibration bead requires a minimally invasive procedure to place the bead initially. Therefore, the utilization of the bead for QUS analysis makes more sense for applications involving ongoing monitoring of tissue state for things, such as detection and quantification of the response of tissue to therapy over time. Radiological markers are already used for these purposes, and clinically, the implantation of a calibration bead for QUS monitoring is not unfeasible.

ACKNOWLEDGMENT

The authors would like to thank Prof. A. Han for reviewing the article.

REFERENCES

- [1] L. Sannachi *et al.*, "Non-invasive evaluation of breast cancer response to chemotherapy using quantitative ultrasonic backscatter parameters," *Med. Image Anal.*, vol. 20, no. 1, pp. 224–236, Feb. 2015.
- [2] R. J. Lavarello, W. R. Ridgway, S. S. Sarwate, and M. L. Oelze, "Characterization of thyroid cancer in mouse models using high-frequency quantitative ultrasound techniques," *Ultrasound Med. Biol.*, vol. 39, no. 12, pp. 2333–2341, 2013.
- [3] E. Feleppa *et al.*, "Three-dimensional ultrasound analyses of the prostate," *Mol. Urol.*, vol. 4, no. 3, pp. 133–139, 2000.
- [4] G. Ghoshal, R. J. Lavarello, J. P. Kemmerer, R. J. Miller, and M. L. Oelze, "Ex vivo study of quantitative ultrasound parameters in fatty rabbit livers," *Ultrasound Med. Biol.*, vol. 38, no. 12, pp. 2238–2248, 2012.
- [5] J. Mamou *et al.*, "Three-dimensional high-frequency backscatter and envelope quantification of cancerous human lymph nodes," *Ultrasound Med. Biol.*, vol. 37, no. 3, pp. 345–357, 2011.
- [6] R. M. Vlad, S. Brand, A. Giles, M. C. Kolios, and G. J. Czarnota, "Quantitative ultrasound characterization of responses to radiotherapy in cancer mouse models," *Clin. Cancer Res.*, vol. 15, no. 6, pp. 2067–2075, 2009.
- [7] M. L. Oelze and J. Mamou, "Review of quantitative ultrasound: Envelope statistics and backscatter coefficient imaging and contributions to diagnostic ultrasound," *IEEE Trans. Ultrason., Ferroelectr., Freq. Control*, vol. 63, no. 2, pp. 336–351, Feb. 2016.
- [8] K. K. Shung, R. A. Sigelmann, and J. M. Reid, "Scattering of ultrasound by blood," *IEEE Trans. Biomed. Eng.*, vol. BME-23, no. 6, pp. 460–467, Nov. 1976.
- [9] F. L. Lizzi, M. Greenebaum, E. J. Feleppa, M. Elbaum, and D. J. Coleman, "Theoretical framework for spectrum analysis in ultrasonic tissue characterization," *J. Acoust. Soc. Amer.*, vol. 73, no. 4, pp. 1366–1373, 1983.
- [10] M. F. Insana, R. F. Wagner, D. G. Brown, and T. J. Hall, "Describing small-scale structure in random media using pulse-echo ultrasound," *J. Acoust. Soc. Amer.*, vol. 87, no. 1, pp. 179–192, 1990.
- [11] R. J. Lavarello, G. Ghoshal, and M. L. Oelze, "On the estimation of backscatter coefficients using single-element focused transducers," *J. Acoust. Soc. Amer.*, vol. 129, no. 5, pp. 2903–2911, 2011.
- [12] L. X. Yao, J. A. Zagzebski, and E. L. Madsen, "Backscatter coefficient measurements using a reference phantom to extract depth-dependent instrumentation factors," *Ultrason. Imag.*, vol. 12, no. 1, pp. 58–70, 1990.
- [13] L. X. Yao, J. A. Zagzebski, and E. L. Madsen, "Statistical uncertainty in ultrasonic backscatter and attenuation coefficients determined with a reference phantom," *Ultrasound Med. Biol.*, vol. 17, no. 2, pp. 187–194, 1991.
- [14] P. Chaturvedi and M. F. Insana, "Error bounds on ultrasonic scatterer size estimates," *J. Acoust. Soc. Amer.*, vol. 100, no. 1, pp. 392–399, 1996.
- [15] M. L. Oelze, J. F. Zachary, and W. D. O'Brien, Jr., "Characterization of tissue microstructure using ultrasonic backscatter: Theory and technique for optimization using a Gaussian form factor," *J. Acoust. Soc. Amer.*, vol. 112, no. 3, pp. 1202–1211, 2002.
- [16] M. L. Oelze and W. D. O'Brien, Jr., "Defining optimal axial and lateral resolution for estimating scatterer properties from volumes using ultrasound backscatter," *J. Acoust. Soc. Amer.*, vol. 115, no. 6, pp. 3226–3234, 2004.
- [17] A. Gerig, J. Zagzebski, and T. Varghese, "Statistics of ultrasonic scatterer size estimation with a reference phantom," *J. Acoust. Soc. Amer.*, vol. 113, no. 6, pp. 3430–3437, 2003.
- [18] Y. Labyed and T. A. Bigelow, "Estimating the total ultrasound attenuation along the propagation path by using a reference phantom," *J. Acoust. Soc. Amer.*, vol. 128, no. 5, pp. 3232–3238, 2010.
- [19] A. L. Coila and R. Lavarello, "Regularized spectral log difference technique for ultrasonic attenuation imaging," *IEEE Trans. Ultrason., Ferroelectr., Freq. Control*, vol. 65, no. 3, pp. 378–389, Mar. 2018.
- [20] Z. Vajjhi, I. M. Rosado-Mendez, T. J. Hall, and H. Rivaz, "Low variance estimation of backscatter quantitative ultrasound parameters using dynamic programming," *IEEE Trans. Ultrason., Ferroelectr., Freq. Control*, vol. 65, no. 11, pp. 2042–2053, Nov. 2018.
- [21] T. A. Bigelow, M. L. Oelze, and W. D. O'Brien, Jr., "Estimation of total attenuation and scatterer size from backscattered ultrasound waveforms," *J. Acoust. Soc. Amer.*, vol. 117, no. 3, pp. 1431–1439, 2005.
- [22] A. D. Pawlicki and W. D. O'Brien, Jr., "Method for estimating total attenuation from a spatial map of attenuation slope for quantitative ultrasound imaging," *Ultrason. Imag.*, vol. 35, no. 2, pp. 162–172, 2013.
- [23] K. A. Wear *et al.*, "Interlaboratory comparison of ultrasonic backscatter coefficient measurements from 2 to 9 MHz," *J. Ultrasound Med.*, vol. 24, no. 9, pp. 1235–1250, 2005.
- [24] F. L. Lizzi, S. K. Alam, S. Mikaelian, P. Lee, and E. J. Feleppa, "On the statistics of ultrasonic spectral parameters," *Ultrasound Med. Biol.*, vol. 32, no. 11, pp. 1671–1685, 2006.
- [25] A. Sadeghi-Naini *et al.*, "Chemotherapy-response monitoring of breast cancer patients using quantitative ultrasound-based intra-tumour heterogeneities," *Sci. Rep.*, vol. 7, no. 1, 2017, Art. no. 10352.
- [26] M. F. Insana, T. J. Hall, and L. T. Cook, "Backscatter coefficient estimation using array transducers," *IEEE Trans. Ultrason., Ferroelectr., Freq. Control*, vol. 41, no. 5, pp. 714–723, Sep. 1994.
- [27] J. Mamou and M. L. Oelze, *Quantitative Ultrasound in Soft Tissues*. Berlin, Germany: Springer, 2013.
- [28] J. J. Faran, Jr., "Sound scattering by solid cylinders and spheres," *J. Acoust. Soc. Amer.*, vol. 23, no. 4, pp. 405–418, 1951.
- [29] K. Nam *et al.*, "Cross-imaging system comparison of backscatter coefficient estimates from a tissue-mimicking material," *J. Acoust. Soc. Amer.*, vol. 132, no. 3, pp. 1319–1324, Sep. 2012.
- [30] K. J. Parker, "Ultrasonic attenuation and absorption in liver tissue," *Ultrasound Med. Biol.*, vol. 9, no. 4, pp. 363–369, 1983.
- [31] J. P. Kemmerer, M. L. Oelze, and M. Gyöngy, "Scattering by single physically large and weak scatterers in the beam of a single-element transducer," *J. Acoust. Soc. Amer.*, vol. 137, no. 3, pp. 1153–1163, 2015.
- [32] N. Kothary *et al.*, "Safety and efficacy of percutaneous fiducial marker implantation for image-guided radiation therapy," *J. Vascular Interventional Radiol.*, vol. 20, no. 2, pp. 235–239, 2009.
- [33] I. Trop, J. David, M. El Khoury, N. Gautier, L. Gaboury, and L. Lalonde, "Microcalcifications around a collagen-based breast biopsy marker: Complication of biopsy with a percutaneous marking system," *Amer. J. Roentgenol.*, vol. 197, no. 2, pp. W353–W357, 2011.

Trong N. Nguyen (M'18) received the M.S. and Ph.D. degrees from the University of Illinois at Urbana-Champaign (UIUC), Urbana, IL, USA, in 2014 and 2019, respectively, all in electrical and electronic engineering.

He is currently a Senior Research Engineer with IGI Medical Technologies, Wheaton, MD, USA. His research interests include quantitative ultrasound, ultrasonic beamformation, machine learning, and augmented reality.

Alex J. Tam, photograph and biography not available at the time of publication.

Minh N. Do (M'01–SM'07–F'14) was born in Vietnam, in 1974. He received the B.Eng. degree in computer engineering from the University of Canberra, Canberra, Australia, in 1997, and the Dr.Sc. degree in communication systems from the Swiss Federal Institute of Technology Lausanne (EPFL), Lausanne, Switzerland, in 2001.

Since 2002, he has been on the faculty with the University of Illinois at Urbana-Champaign (UIUC), Urbana, IL, USA, where he is currently a Professor with the Department of Electrical and Computer Engineering and holds joint appointments with the Coordinated Science Laboratory, Urbana, the Beckman Institute for Advanced Science and Technology, Urbana, the Advanced Digital Sciences Center, Singapore, the Department of Bioengineering, and the Department of Computer Science. He was a co-founder and a CTO of Personify, Inc., a spin-off from UIUC to commercialize depth-based visual communication. His research interests include signal processing, computational imaging, geometric vision, and data science.

Prof. Do was a Member of the IEEE Signal Processing Theory and Methods Technical Committee and the Image, Video, and Multidimensional Signal Processing Technical Committee. He was a recipient of the Silver Medal from the 32nd International Mathematical Olympiad in 1991, the University Medal from the University of Canberra in 1997, the Doctorate Award from the EPFL in 2001, the CAREER Award from the National Science Foundation in 2003, and the Young Author Best Paper Award from the IEEE in 2008. He was named a Beckman Fellow with the Center for Advanced Study, UIUC, in 2006, and received the Xerox Award for Faculty Research from the College of Engineering, UIUC, in 2007. He was an Associate Editor of the IEEE TRANSACTIONS ON IMAGE PROCESSING.

Michael L. Oelze (M'03–SM'09) was born in Hamilton, New Zealand, in 1971. He received the B.S. degree in physics and mathematics from Harding University, Searcy, AR, USA, in 1994, and the Ph.D. degree in physics from the University of Mississippi, Oxford, MS, USA.

From 2000 to 2002, he was a Postdoctoral Researcher with the Bioacoustics Research Laboratory, Department of Electrical and Computer Engineering (ECE), University of Illinois at Urbana-Champaign (UIUC), Urbana, IL, USA. From 2002 to 2004, he was an NIH Fellow conducting research in quantitative ultrasound techniques for biomedical ultrasound applications in cancer detection. In 2005, he joined the Faculty Member of the ECE, UIUC, where he is currently a Professor and the Associate Head for Graduate Affairs. His research interests include biomedical ultrasound, quantitative ultrasound imaging for improving cancer diagnostics and monitoring therapy response, ultrasound bio-effects, ultrasound tomography techniques, ultrasound-based therapy, beamforming, and applications of coded excitation to ultrasonic imaging.

Dr. Oelze is currently a Fellow of the AIUM, and a Member of ASA and the Technical Program Committee of the IEEE Ultrasonics Symposium. He also serves as an Associate Editor for the IEEE TRANSACTIONS ON ULTRASONICS, FERROELECTRICS, AND FREQUENCY CONTROL, *Ultrasonic Imaging*, and IEEE TRANSACTIONS ON BIOMEDICAL ENGINEERING.